Micro and Macroscopic Stress-Strain Relations in Disordered Tessellated Networks

Ran Li, Seyedsajad Moazzeni, Liping Liu, and Hao Lin

Phys. Rev. Lett. **130**, 188201 — Published 3 May 2023

DOI: 10.1103/PhysRevLett.130.188201

Micro- and macro-scopic stress-strain relations in disordered tessellated networks

Ran Li,[1] Seyedsajad Moazzeni,[1] Liping Liu,[1, 2] and Hao Lin[1, *]
[1] *Department of Mechanical and Aerospace Engineering,*
Rutgers, The State University of New Jersey
[2] *Department of Mathematics,*
Rutgers, The State University of New Jersey
(Dated: March 7, 2023)

We demonstrate that for a rigid and incompressible network in mechanical equilibrium, the microscopic stress and strain follows a simple relation, $\sigma = p\mathbf{E}$, where σ is the deviatoric stress, $\mathbf{E}$ is a mean-field strain tensor, and p is the hydrostatic pressure. This relationship arises as the natural consequence of energy minimization or equivalently, mechanical equilibration. The result suggests not only that the microscopic stress and strain are aligned in the principal directions, but also microscopic deformations are predominantly *affine*. The relationship holds true regardless of the different (foam or tissue) energy model considered, and directly leads to a simple prediction for the shear modulus, $\mu = \langle p \rangle /2$, where $\langle p \rangle$ is the mean pressure of the tesselation, for general randomized lattices.

INTRODUCTION

Soft network materials, such as liquid foams and epithelial tissues, are drawing increasing attention due to broad applications in the materials, physical, and biological contexts [1, 2]. Control of constituting cells (in the broad sense) in the network enables complex macroscopic behavior, and cellular properties often dictate global processes such as rigidity transition, flow, and embryonic morphogenesis [3–5]. Among the considerations the mechanical state and properties are of particular importance. For liquid foams, they are essential properties that directly impact industrial applications [6], and a body of literature exists in analyzing and predicting the moduli and general rheological behavior [7–11]. For biological tissue mechanical cues and feedbacks drive cell rearrangements, direct morphogenesis, and help establish tension homeostasis [3, 4, 12, 13]. Prior efforts tackled tissue mechanics using specific energy models, and significant progress have been made by various studies [4, 14–18]. On the other hand, quantitative understanding remains limited due to challenges in mathematical analysis.

Despite the disordered nature and complexity of the networks, one can often explore consistent patterns and correlations, such as the classical Lewis and Weaire-Aboav laws, and more recently universal distributions in cell shapes [19–22]. These findings provide both strong mathematical-physical insights and system constraints, which can be harnessed to advance analysis. Here we illuminate one such embedded correlation, between the microscopic, cell-wise stress and strain in planar tesselated networks. This relationship is valid within the rigid regime where the network is more similar to an elastic solid in mechanical responses, which includes most foam structures and biological tissue with lower adhesion strengths. We demonstrate that it is a natural consequence of energy minimization, and furthermore, that microscopic deformations are predominantly *affine*. On the macroscopic level, an average of the local strain quantitatively predicts the global deformation, whereas the stress-strain relation immediately leads to a simple, unifying formula for the shear modulus of randomized lattices. We verify all results with numerical simulations.

RESULTS

We begin by introducing the microscopic, cell-wise strain tensor, $\mathbf{E}$, following our prior work [22]. In the schematic (Fig. 1), a regular n-polygon with the same geometric center (point O) and area, $\mathcal{P}_R$, is chosen as the reference for each polygon $\mathcal{P}$. Note that this reference is chosen for each individual polygon to quantify their deviation from a regular shape, and the $\mathcal{P}_R$s altogether do not tessellate the plane. The strain tensor $\mathbf{E}$ is obtained via best approximating the deformation from $\mathcal{P}_R$ to $\mathcal{P}$ under least-square minimization. While we previously derived $\mathbf{E}$ in terms of coordinates of the vertices, in the current work it is convenient to express $\mathbf{E}$ with respect to the edge vectors,

$$\mathbf{E} = \frac{1}{nl_0^2}\sum_{k=1}^{n}(\delta\mathbf{l}_k \otimes \mathbf{l}_k^0 + \mathbf{l}_k^0 \otimes \delta\mathbf{l}_k), \tag{1}$$

where $\mathbf{l}_k^0$ and $\mathbf{l}_k$ are the edge vectors of $\mathcal{P}$ and $\mathcal{P}_R$, respectively, defined in counter-clockwise manner. $\delta\mathbf{l}_k$ is their difference, $\delta\mathbf{l}_k := \mathbf{l}_k - \mathbf{l}_k^0$. l_0 is the edge length of $\mathcal{P}_R$. We will show below that on the tesselation level $\mathbf{E}$ is equivalent to the texture strain [10] and reflects the true strain.

For stress we use the well-established virial stress [14, 15, 23–26]; the microscopic, cell-wise version is written

---

* Corresponding author: hlin@soe.rutgers.edu

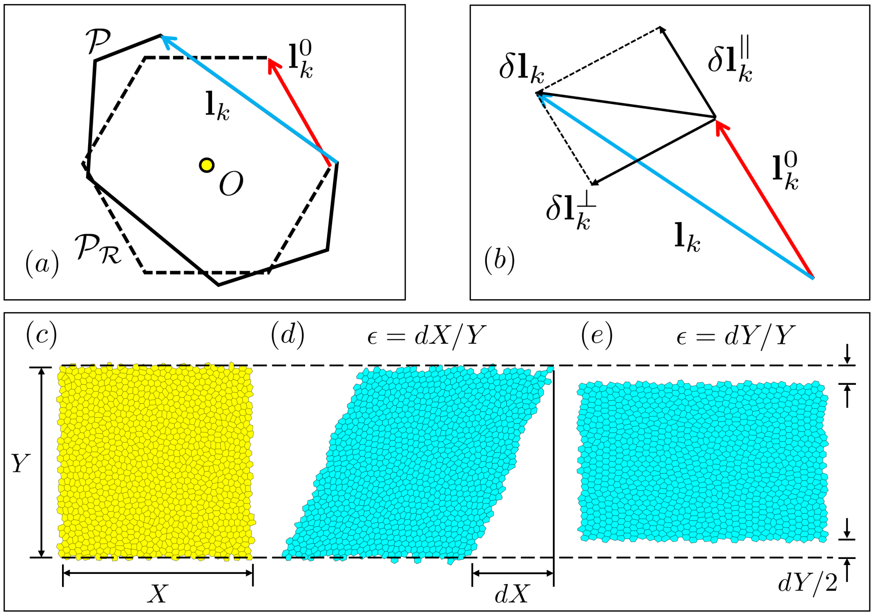

FIG. 1. (a) A schematics of polygon deformation. $\mathcal{P}$ is a polygon from a tessellation, $\mathcal{P}_\mathcal{R}$ is the reference regular n-gon with the same area and geometric center (O). (b) Edge displacement vector decomposition. (c) An undeformed tessellation in mechanical equilibrium. Two different types of shear are applied to the tessellation: (d) Shear Type-1 (simple shear), and (e) Shear Type-2 (pure shear).

as

$$\tau = \frac{1}{A}\sum_{k=1}^{n} \lambda \frac{\mathbf{l}_k}{l_k} \otimes \mathbf{l}_k. \tag{2}$$

Here A is polygon area, $l_k := |\mathbf{l}_k|$, and λ is the tension assigned to each polygon (further specified below). In the current case because the network is static and in equilibrium, summation of τA over the tesselation and normalized by total area provides the true mechanical stress [15]. The relationship between τ and $\mathbf{E}$ becomes evident, and via a Taylor expansion we have (Supplemental Information):

$$\tau = \frac{\lambda P_0}{2A}(\mathbf{I} + \mathbf{E} + \mathbf{E}^{\perp}) + \mathcal{O}(\delta^2), \tag{3a}$$

$$\mathbf{E}^{\perp} := \frac{1}{n l_0^2}\sum_{k=1}^{n}(\delta \mathbf{l}_k^{\perp} \otimes \mathbf{l}_k^0 + \mathbf{l}_k^0 \otimes \delta \mathbf{l}_k^{\perp}), \tag{3b}$$

where $P_0 = n l_0$ and is the perimeter of the reference regular n-gon, and $\delta \mathbf{l}_k^{\perp}$ is the projection of $\delta \mathbf{l}_k$ in the direction normal to $\mathbf{l}_k^0$, namely $\delta \mathbf{l}_k^{\perp} := \delta \mathbf{l}_k - (\delta \mathbf{l}_k \cdot \mathbf{l}_k^0)\mathbf{l}_k^0/l_0$ (see Fig. 1b). Following convention we term $\delta \mathbf{l}^{\perp}$ *non-affine* deformation [27–29]. We immediately realize that the hydrostatic pressure is precisely of the Young-Laplace form,

$$p = \lambda/R_0, \quad R_0 = 2A/P_0, \tag{4}$$

with the effective radius of curvature R_0 being half of the two-dimensional Sauter mean diameter of the regular polygon $\mathcal{P}_R$. Note that by convention p assumes a negative sign, but here we define p as a positive quantity for convenience. A further key realization is that for an energy-minimized tessellation in the rigid (versus "floppy") regime, $|\mathbf{E}^{\perp}| \ll |\mathbf{E}|$, hence the deviatoric stress is related to the strain as

$$\sigma = p\mathbf{E}. \tag{5}$$

In this work, we restrict to area-preserving (incompressible) deformations and hence both σ and $\mathbf{E}$ are trace-free. Equation (5) is a key result of the current work.

We validate these results with extensive numerical simulations using Surface Evolver [30]. Table I summarizes the number of randomized tessellations, each subject to different models and externally imposed deformation (for two different shear types in Fig. 1). We test two different energy models on each tessellation, namely,

$$E_f = \frac{1}{2}\sum_{\alpha} \beta P_\alpha; \tag{6}$$

$$E_t = \sum_{\alpha} \frac{\left[P_\alpha - (1 + \gamma/2)\, P_{c,\alpha}\right]^2}{2 P_{c,\alpha}}. \tag{7}$$

Following literature, we term (6) the "foam model" [31–35] and (7) the "tissue model" [36–42], reflected by the subscripts. P is polygon perimeter, and α is polygon

TABLE I. Tessellations are tested in numerical simulation, with standard deviation of cell area c_A denotes polydispersity (standard deviation of cell area). Both foam and tissue models are implemented on each tessellation for subsequent energy minimization (Eqs (6), (7)). Subsets of load-free tesselations are subject to macroscopic shears (Fig. 1d, e).

Polydispersity:	Number of Generated Tessellations		
$c_A = \mathrm{std}\,(A)$	Load-free	Shear Type-1	Shear Type-2
0	40	5	5
0.1	40	5	5
0.2	40	5	5

index. In (6) β is the constant edge tension, and $\lambda = \beta/2$ for (2). The factor of 1/2 arises as we distribute the tension equally to neighboring polygons. For the tissue model (7) γ represents adhesion, e.g., that mediated by cadherins, and is normalized following [12]. $P_{c,\alpha}$ is a reference perimeter for each polygon. (Note that P_c is different than P_0, the perimeter of the regular polygon; see details in SI [43].) The contribution of each polygon toward edge tension is

$$\lambda_\alpha = P_\alpha / P_{c,\alpha} - 1 - \gamma/2, \tag{8}$$

and adding λ_α for the neighboring polygons sharing an edge provides the total edge tension. Notably, Eqs. (6) and (7) can be considered the (up to) first- and second-order Taylor expansions of a more complex energy functional, respectively [44]. Hence unless the involvement of third-order terms or higher are strongly justified, they encompass a broad class of situations. The justification of using (7) to study biological tissue is presented elsewhere [3, 4, 12, 14, 15, 21, 25, 36–38, 40–42, 44–52] and not repeated here.

Figure 2 compiles results from all 600 simulations after energy minimization, including three levels of polydispersity, both the foam and tissue energy models, and all the load-free and shear types. (details of cases included for this and the following figures are described in SI [43]). Polygon areas are kept at constant values during energy minimization. For the tissue model, we restrict to the rigid regime with $\gamma = 0, 0.05$, and 0.1. Behavior in the so-called "floppy" regime is discussed later. Figure 2a verifies the accuracy of Eq. (4), namely, the Laplace-Young relation. Here p is computed directly by assessing the isotropic part of tensor τ per (2) and compared with λ/R_0 for all individual polygons in all tessellations. The panel shows results with the tissue model, whereas the inset is with the foam model. Figure 2b validates the deviatoric relation (5). Only the two components of the tensors are shown. whereas the others are dependent via trace-free condition and symmetry. Evidently, the slight scatter is due to the higher-order fluctuations caused by a small yet non-zero $\mathbf{E}^\perp$.

We next demonstrate that minimization of $|\mathbf{E}^\perp|$ is a consequence of energy minimization, and also that this conclusion is particular to the rigid regime. Figure 3a shows $\left\langle|\delta\mathbf{l}^\perp|^2\right\rangle / \left\langle|\delta\mathbf{l}|^2\right\rangle$ as a function of iteration step during the energy minimization process for both the foam model and for $\gamma = 0.05$, 0.15, and 0.25 with the tissue model, with and without deformation ($n = 11$ each). The brackets $\langle\cdot\rangle$ indicate averaging over the tessellation. The initial step represents the non-minimized original lattice. For the foam and tissue models with $\gamma \le 0.15$, $\left\langle|\delta\mathbf{l}^\perp|^2\right\rangle / \left\langle|\delta\mathbf{l}|^2\right\rangle$ rapidly decreases to a small value as iteration proceeds; whereas for $\gamma = 0.25$ it remains at a relatively larger value. Figure 3b shows similar trends with $\left\langle|\mathbf{E}^\perp|^2\right\rangle / \left\langle|\mathbf{E}|^2\right\rangle$; the agreement with $\left\langle|\delta\mathbf{l}^\perp|^2\right\rangle / \left\langle|\delta\mathbf{l}|^2\right\rangle$ is expected per definitions of $\mathbf{E}^\perp$ and $\mathbf{E}$.

On the other hand, these trends are only true in the so-called rigid regime. Figure 3c demonstrates the behavior of the non-affine displacement as a function of γ, the adhesion strength which mediates rigidity transition. We observe that the magnitude of $\delta\mathbf{l}^\perp$ in general increases with c_A, but nevertheless remains small and relatively constant for $\gamma \le 0.15$. Beyond $\gamma = 0.15$ the increase substantially for all c_A values. The transition from rigid to floppy regime concurs with prior work quantitatively [12, 36] and in the latter the line tension becomes effectively 0 (Fig. S2).

Taken together, these results lead to two important observations, that *(i)* in mechanical equilibrium the deformations are mostly *affine*; namely, the edges primarily stretch along the directions of the reference regular polygon edges (see SI for further details [43]), and *(ii)* the microscopic stress and strain are aligned in the principal directions. We interpret these results via a detailed examination of the polygon perimeter. Writing P in Taylor expansion with respect to regular polygon P_0 and considering the trace-free condition, $\sum_{k=1}^{n} \delta\mathbf{l}_k \cdot \mathbf{l}_k^0 = 0$, we have (SI [43]) for each polygon

$$P = P_0 \left(1 + \frac{1}{2nl_0^2} \sum_{k=1}^{n} |\delta\mathbf{l}_k^\perp|^2 \right). \tag{9}$$

Since P_0 is a constant given a constant polygon area, minimization of an energy functional based on perimeter hence necessarily leads to the minimization of $|\delta\mathbf{l}_k^\perp|$, which subsequently leads to that of $|\mathbf{E}^\perp|$. The different behavior in the floppy regime, on the other hand, can be explained following the work of Damavandi et al. [53], where the presence of floppy modes allows further degrees of freedom for the non-affine displacements to "jiggle around" and to achieve greater magnitude, instead of settling down to defined minima. (Note that our definition of $\delta\mathbf{l}^\perp$ is similar to that in [53] but with a subtle difference in the reference framework.) In this sense, the non-affine modes are analogous to thermal fluctuations in a solid-liquid phase (rigidity) transition.

In the next part, we show that the above results immediately lead to predictions on macroscopic mechanical properties. On the tessellation level, the deviatoric part

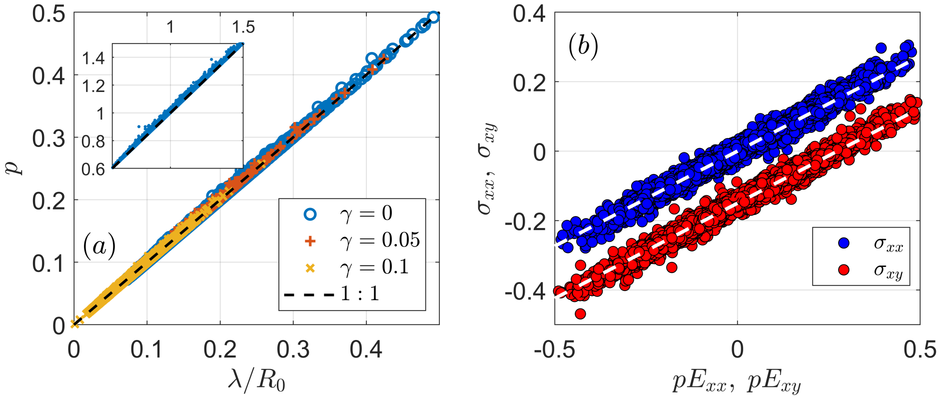

FIG. 2. (a) The isotropic (hydrostatic) stress obeys the Young-Laplace relation, $p = \lambda/R_0$. Results from the foam model is shown as inset due to the difference in value range. (b) The deviatoric tensors obey $\sigma = p\mathbf{E}$. The dashed line represents 1 : 1. The off-diagonal component is shifted artificially downward for better visualization and otherwise the two data sets completely overlap.

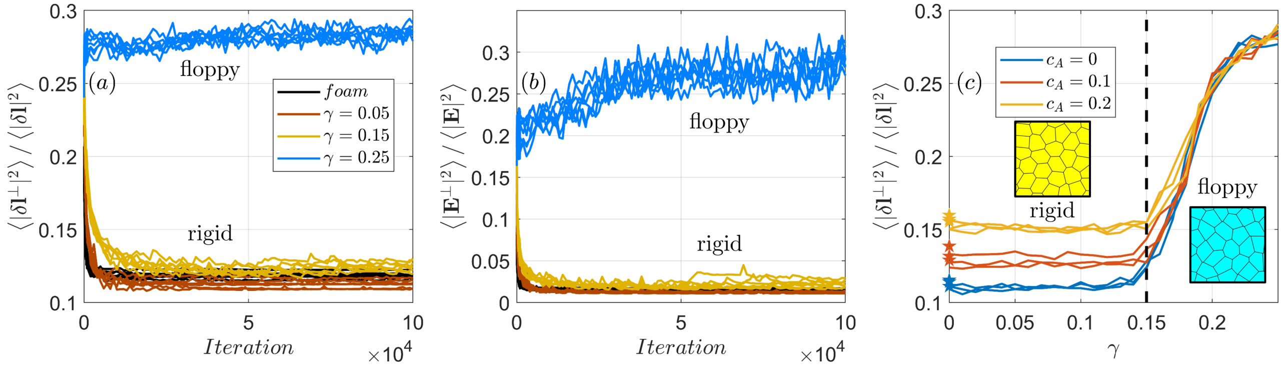

FIG. 3. (a) In the rigid regime the relative magnitude of non-affine displacement, $\delta\mathbf{l}^{\perp}$ decreases as energy minimizes, which leads to (b) a similar decrease in that of $\mathbf{E}^{\perp}$. In the floppy regime, however, they remain significant or even increase. (c) Non-affine displacement as a function of adhesion strength, γ, demonstrating regime transition. The stars represent data from a foam model with the same tessellation.

of the virial stress, Σ, is related to σ as

$$\Sigma = \frac{1}{A_{tot}} \sum_{\alpha} A_{\alpha} \sigma_{\alpha},$$

where α is an index for polygon, and A_{tot} is the total tessellation area. For simplicity, we first consider a monodispersed isotropic foam, where λ is constant and $\Sigma = \langle p\mathbf{E} \rangle$. For this case, p only depends on n, the number of polygon edges. If we assume that p and $\mathbf{E}$ are not correlated, then $\Sigma \approx \langle p \rangle \langle \mathbf{E} \rangle$, and the shear modulus, μ, is obtained as

$$\mu = \langle p \rangle /2. \qquad (10)$$

Note we can also similarly derive the Youngs modulus, $Y = 2\langle p \rangle$, which is consistent with the relationship $Y = 4\mu$ for 2D incompressible elastic solids (SI [43]). Here we assume that $\langle \mathbf{E} \rangle$ provides the macroscopic strain, which is to be verified below. In case of a regular honeycomb structure, the result recovers precisely the classical result of Princen [24, 54]: the prediction of μ is $0.931\lambda/\sqrt{A}$ and $0.930\lambda/\sqrt{A}$ from (10) and [54], respectively (SI [43]). Eq. (10) is also consistent with [55] where the result is derived assuming also a regular honeycomb structure and infinitely compliant edges. However, in our theory the assumption that p and $\mathbf{E}$ are not (in actuality, weakly) correlated is readily generalized, which generalizes (10) in the broadest sense, namely, for all *randomized*, *polydispersed*, and *isotropic/moderately-anisotropic* lattices. This we numerically validate.

We first demonstrate that the tessellation-level mean of $\mathbf{E}$ indeed represents the microscopic strain. Fig. 4a shows $\langle \delta E \rangle$ as a function of ϵ, where all cases pertaining to both shear types from Table 1 are included. Both foam model and tissue model with $\gamma = 0.05$ are included. Here $\delta\mathbf{E} = \mathbf{E} - \mathbf{E}_0$, where the subscript denotes strain in the un-deformed state. Although $\mathbf{E}_0 \approx 0$ for the initial isotropic state, the small numerical residue is corrected

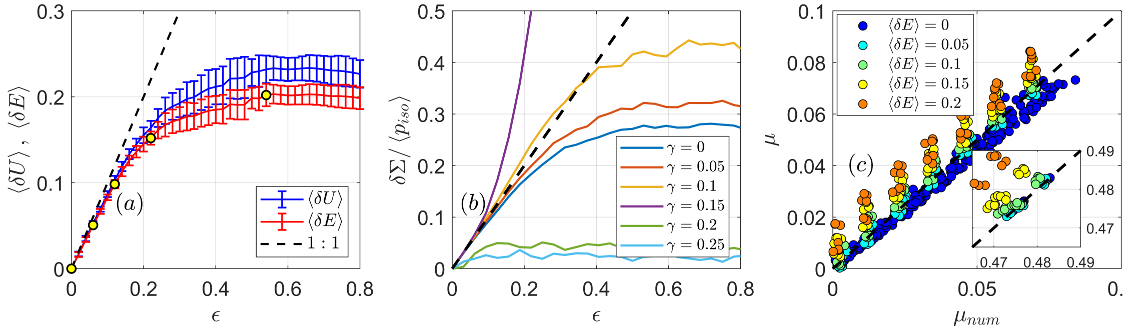

FIG. 4. (a) The averaged strain magnitude $\langle \delta E \rangle$ captures the macroscopic strain, ϵ in the linear regime. As a reference, $\langle \delta U \rangle$ is the so-called "texture strain" from [10]. (b) Stress-strain relation, where p_{iso} denotes pressure evaluated in the un-deformed, isotropic state. (c) Validation of (10) against numerically evaluated modulus for both isotropic ($\langle \mathbf{E} \rangle = 0$) and anisotropic ($\langle \mathbf{E} \rangle > 0$) lattices; inset shows foam model where the lattices has much greater moduli.

for rigor. The scalar E is taken to be E_{xy} for shear type-1 and E_{xx} for type-2, respectively. For reference, we also show the same components of $\mathbf{U}$, which is historically known as the "texture" tensor [10]. The results demonstrate that both $\langle \mathbf{E} \rangle$ and $\langle \mathbf{U} \rangle$ well-captures the macroscopic strain ϵ, in particular in the small-deformation regime. Indeed, we can demonstrate that these two strains are equivalent to leading order (SI [43]). However, the simple and concise form of $\mathbf{E}$ (Eq. (1)) provides convenience in both computation and understanding. Between $\epsilon = 0.2$ and 0.4, the system transitions to the plastic regime where externally imposed shear no longer induces commensurate microscopic strain.

Fig. 4b shows $\delta\Sigma / \langle p_{iso} \rangle$ against ϵ for both shear types, where $\delta\Sigma$ is similarly defined as δE. Here $\langle p_{iso} \rangle$ denotes pressure evaluated in the isotropic state, namely, prior to shear application, which therefore is a constant that does not vary with ϵ. For rigid lattices ($\gamma = 0, 0.05, 0.1$) again two clear regimes are observed as ϵ increases: linear elastic, followed by plastic which demonstrates approximate constant stress [42]. For floppy lattices $\gamma \gtrsim 0.15$ no definitive stress-strain relationship is observed due to fluid-like behavior. Importantly, the linearity for rigid tessellations confirms that $\langle p_{iso} \rangle / 2$ is a good representation of shear modulus for both isotropic and moderately anisotropic lattices; results show that deviation becomes appreciable for $\epsilon \gtrsim 0.3$. This trend is better observed in Fig. 4c, where we compare numerically obtained (by evaluating $\partial\Sigma / 2\partial\epsilon$) modulus, μ_{num}, against μ, evaluated from $\langle p_{iso} \rangle / 2$. For isotropic lattices, the agreement is near perfect. For anisotropic lattices, theoretical predictions are great for $\langle E \rangle$ up to 0.1. Note that here we switch to $\langle E \rangle$ as it is directly computable given any tessellation while ϵ is externally imposed, and the correponding values are marked as yellow circles in Fig. 4a. We observe that $\langle E \rangle$ =0.15 is in the transition zone, whereas $\langle E \rangle$ =0.2 is well in the plastic regime. Prediction of modulus in these regimes are of greater complexity and will be explored in future work.

Some technicality is involved in evaluating p_{iso}: while in our simulations the isotropic lattice is known, how does one "back"-calculate p_{iso} given any anisotropic lattice? This is done by utilizing $P \approx P_{iso}(1 + (|\mathbf{E}|^2 - |\mathbf{E}_{iso}|^2)/4)$ which was obtained in our prior work via Taylor expansion [22] (*c.f.* Eq. (2) in [42] which was obtained empirically). Namely, the relative difference in perimeter due to isochoric deformation is given by $\delta|\mathbf{E}|^2/4$ to the leading order. Utilizing these relations for p, we obtain

$$\langle p_{iso} \rangle \approx \langle p \rangle - \left\langle \frac{P_0 P}{8 P_c A} \right\rangle |\mathbf{E}|^2, \tag{11}$$

assuming $|\mathbf{E}_{iso}|^2 \approx 0$. Figure S3 demonstrates that (11) provides a very good approximation for p_{iso}, hence also for μ up to moderate anisotropy.

CONCLUSION

In summary, we have unveiled a general correlation embedded in tessellated systems in the rigid regime: on the grain level, the main mode of deformation is affine, and stress and strain behave very similarly to linear elastic material despite the disordered nature of the system. On the tessellation level, we present a simple, physically meaningful, and unifying formula for the elastic modulus that is broadly applicable to tessellated systems. Note that although we did not include an areal change term as in prior work [12, 14, 36, 38, 46], such term would only contribute an additional component in the isotropic part of the stress, and does not alter the quantitative results above. Evidently, the non-affine displacement $\delta \mathbf{l}^{\perp}$ is an indicating quantity that behaves distinctively different in the rigid and floppy regimes, and we intend to further investigate its behavior and pertinence to phase transition in future work. Last but not least, although the current work only investigated planar tessellations, we imagine similar patterns may persist in three-dimensional, space-partitioned structures.

The authors acknowledge funding support from NIH Grant No. R21 CA220202-02 [principal investigator (PI): H.L.]; NSF Grant No. CMMI 1351561 and No. DMS 1410273 (PI: L.L.). The authors acknowledge helpful suggestions from an anonymous reviewer.

---

[1] W. Drenckhan and S. Hutzler, Advances in Colloid and Interface Science **224**, 1 (2015).
[2] T. Lecuit and P.-F. Lenne, Nat. Rev. Mol. Cell. Biol. **8**, 633 (2007).
[3] A. Mongera, P. Rowghanian, H. J. Gustafson, E. Shelton, D. A. Kealhofer, E. K. Carn, F. Serwane, A. A. Lucio, J. Giammona, and O. Campàs, Nature **561**, 401 (2018).
[4] X. Wang, M. Merkel, L. B. Sutter, G. Erdemci-Tandogan, M. L. Manning, and K. E. Kasza, Proc. Natl. Acad. Sci. USA **117**, 13541 (2020).
[5] M. L. Manning, R. A. Foty, M. S. Steinberg, and E.-M. Schoetz, Proc. Natl. Acad. Sci. USA **107**, 12517 (2010).
[6] R. Höhler and S. Cohen-Addad, J. Phys.: Condens. Matter **17**, R1041 (2005).
[7] S. A. Khan and R. C. Armstrong, J. Non-Newton. Fluid Mech. **22**, 1 (1986).
[8] D. Stamenovic, J. Colloid Interface Sci. **145**, 255 (1991).
[9] D. Weaire and T. L. Fu, J. Rheol. **32**, 271 (1988).
[10] M. Aubouy, Y. Jiang, J. A. Glazier, and F. Graner, Granul. Matter **5**, 67 (2003).
[11] N. P. Kruyt, J. Appl. Mech. **74**, 560 (2007).
[12] S. Kim and S. Hilgenfeldt, Soft Matter **11**, 7270 (2015).
[13] S. Moazzeni, Y. Demiryurek, M. Yu, D. I. Shreiber, J. D. Zahn, J. W. Shan, R. A. Foty, L. Liu, and H. Lin, Phys. Rev. E **103**, 032409 (2021).
[14] A. Nestor-Bergmann, E. Johns, S. Woolner, and O. E. Jensen, Phys. Rev. E **97**, 052409 (2018).
[15] A. Nestor-Bergmann, G. Goddard, S. Woolner, and O. E. Jensen, Math. Med. Biol. J. IMA **35**, i1 (2018).
[16] L. Yan and D. Bi, Phys. Rev. X **9**, 011029 (2019).
[17] D. Staple, R. Farhadifar, J. C. Röper, B. Aigouy, S. Eaton, and F. Jülicher, Eur. Phys. J. E: Soft Matter Biol. Phys. **33**, 117 (2010).
[18] M. Krajnc, S. Dasgupta, P. Ziherl, and J. Prost, Phys. Rev. E **98**, 022409 (2018).
[19] S. N. Chiu, Mater. Charact. **34**, 149 (1995).
[20] M. P. Miklius and S. Hilgenfeldt, Phys. Rev. Lett. **108**, 015502 (2012).
[21] L. Atia, D. Bi, Y. Sharma, J. A. Mitchel, B. Gweon, S. A. Koehler, S. J. DeCamp, B. Lan, J. H. Kim, R. Hirsch, A. F. Pegoraro, K. H. Lee, J. R. Starr, D. A. Weitz, A. C. Martin, J.-A. Park, J. P. Butler, and J. J. Fredberg, Nat. Phys. **14**, 613 (2018).
[22] R. Li, C. Ibar, Z. Zhou, S. Moazzeni, A. N. Norris, K. D. Irvine, L. Liu, and H. Lin, Phys. Rev. Research **3**, L042001 (2021).
[23] D. H. Tsai, J. Chem. Phys. **79**, 1375 (1979).
[24] S. Courty, B. Dollet, F. Elias, P. Heinig, and F. Graner, Euro. Phys. Lett. , 8 (2003).
[25] X. Yang, D. Bi, M. Czajkowski, M. Merkel, M. L. Manning, and M. C. Marchetti, Proc. Natl. Acad. Sci. USA **114**, 12663 (2017).
[26] J. Tauber, *Dealing with stress: elasticity and fracture of soft network materials*, Ph.D. thesis, Wageningen University and Research (2021).
[27] W. G. Ellenbroek, E. Somfai, M. van Hecke, and W. van Saarloos, Phys. Rev. Lett. **97**, 258001 (2006).
[28] B. A. DiDonna and T. C. Lubensky, Phys. Rev. E **72**, 066619 (2005).
[29] S. Chen, T. Markovich, and F. C. MacKintosh, arXiv:2206.09052 (2022).
[30] K. Brakke, Exp. Math. **1**, 141 (1992).
[31] M. Durand and H. A. Stone, Phys. Rev. Lett. **97**, 226101 (2006).
[32] M. Durand, J. Käfer, C. Quilliet, S. Cox, S. A. Talebi, and F. Graner, Phys. Rev. Lett. **107**, 168304 (2011).
[33] M. Durand and J. Heu, Phys. Rev. Lett. **123**, 188001 (2019).
[34] A. Kabla and G. Debrégeas, Phys. Rev. Lett. **90**, 258303 (2003).
[35] A. L. Biance, A. Delbos, and O. Pitois, Phys. Rev. Lett. **106**, 068301 (2011).
[36] D. Bi, J. H. Lopez, J. M. Schwarz, and M. L. Manning, Nat. Phys. **11**, 1074 (2015).
[37] D. Bi, X. Yang, M. C. Marchetti, and M. L. Manning, Phys. Rev. X **6**, 021011 (2016).
[38] S. Kim, Y. Wang, and S. Hilgenfeldt, Phys. Rev. Lett. **120**, 248001 (2018).
[39] B. Loewe, M. Chiang, D. Marenduzzo, and M. C. Marchetti, Phys. Rev. Lett. **125**, 038003 (2020).
[40] D. M. Sussman, J. M. Schwarz, M. C. Marchetti, and M. L. Manning, Phys. Rev. Lett. **120**, 058001 (2018).
[41] S. M. Fielding, J. O. Cochran, J. Huang, D. Bi, and M. C. Marchetti, ArXiv:2210.02893 (2022).
[42] J. Huang, J. O. Cochran, S. M. Fielding, M. C. Marchetti, and D. Bi, Phys. Rev. Lett. **128**, 178001 (2022).
[43] See Supplemental Material at [URL will be inserted by publisher] for supplemental results and some details of the mathematical derivation which compements the main text, which includes Refs. [56–58].
[44] M. L. Manning, R. A. Foty, M. S. Steinberg, and E. Schoetz, Proc. Natl. Acad. Sci. USA **107**, 12517 (2010).
[45] M. Merkel and M. L. Manning, New J. Phys. **20**, 022002 (2018).
[46] R. Farhadifar, J. Röper, B. Aigouy, S. Eaton, and F. Jülicher, Curr. Biol. **17**, 2095 (2007).
[47] A. Hernandez, M. F. Staddon, M. J. Bowick, M. C. Marchetti, and M. Moshe, Phys. Rev. E **105**, 064611 (2022).
[48] S. Z. Lin, B. Li, G. K. Xu, and X. Q. Feng, J. Biomech. **52**, 140 (2017).
[49] L. Oswald, S. Grosser, D. M. Smith, and J. A. Käs, J. Phys. D: Appl. Phys. **50**, 483001 (2017).
[50] P. Mosaffa, R. J. Tetley, A. Rodríguez-Ferran, Y. Mao, and J. J. Muñoz, J. R. Soc. Interface **17**, 20200264 (2020).
[51] M. F. Staddon, D. Bi, A. P. Tabatabai, V. Ajeti, M. P. Murrell, and S. Banerjee, PLoS Comput. Biol. **14**, e1006502 (2018).
[52] C. P. Heisenberg and Y. Bellaïche, Cell **153**, 948 (2013).
[53] O. K. Damavandi, V. F. Hagh, C. D. Santangelo, and M. L. Manning, arXiv (2021).
[54] H. M. Princen, J. Colloid Interface Sci. **91**, 16 (1983).
[55] T. A. Wilson, J. Appl. Physiol. **33**, 472 (1972).
[56] S. J. Cox and E. L. Whittick, Eur. Phys. J. E **21**, 49 (2006).

[57] J. R. Iglesias and R. M. C. de Almeida, Phys. Rev. A **43**, 2763 (1991).

[58] S. Kim, M. Cai, and s. Hilgenfeldt, New J. Phys. **16**, 015024 (2014).